

Superconductivity in YRu_3B_2 and LuRu_3B_2

Rose Albu Mustaf,^{1, 2,*} Sajilesh K. P.,^{1, 2,*} Sanu Mishra,^{1, 2} Junze Deng,³ Yi Jiang,⁴ Kaja H. Hiorth,³ Eeli O. Lamponen,³ Martin Gutierrez-Amigo,³ Päivi Törmä,³ Miguel A.L. Marques,⁵ B. Andrei Bernevig,^{4, 6, 7} and Emilia Morosan^{1, 2, †}

¹*Department of Physics and Astronomy, Rice University, Houston, Texas 77005, USA*

²*Rice Center for Quantum Materials, Rice University, Houston, Texas 77005, USA*

³*Department of Applied Physics, Aalto University School of Science, FI-00076 Aalto, Finland*

⁴*Donostia International Physics Center (DIPC), Paseo Manuel de Lardizábal. 20018, San Sebastián, Spain*

⁵*Research Center Future Energy Materials and Systems of the University Alliance Ruhr and Interdisciplinary Centre for Advanced Materials Simulation, Ruhr University Bochum, Universitätsstraße 150, D-44801 Bochum, Germany*

⁶*Department of Physics, Princeton University, Princeton, NJ 08544, USA*

⁷*IKERBASQUE, Basque Foundation for Science, 48013 Bilbao, Spain*

(Dated: December 22, 2025)

We report the experimental discovery of bulk superconductivity in two kagome lattice compounds, YRu_3B_2 and LuRu_3B_2 , which were predicted through machine learning-accelerated high-throughput screening combined with first principles calculations. These materials crystallize in the hexagonal CeCo_3B_2 -type structure with planar kagome networks formed by Ru atoms. We observe superconducting critical temperatures of $T_c = 0.81$ K for YRu_3B_2 and $T_c = 0.95$ K for LuRu_3B_2 , confirmed through magnetization and specific heat measurements. Both compounds exhibit nearly 100% superconducting volume fractions, demonstrating bulk superconductivity. Compared with LaRu_3Si_2 , YRu_3B_2 and LuRu_3B_2 show a more dispersive Ru local $d_{x^2-y^2}$ quasi-flat band (and thus a reduced DOS at E_F) together with an overall hardening of the phonon spectrum, both of which lower the electron-phonon coupling (EPC) constant λ . Meanwhile, the dominant real-space EPC between Ru local $d_{x^2-y^2}$ states and the low-frequency Ru in-plane local x branch remains nearly unchanged, indicating that the reduction of λ originates from the $d_{x^2-y^2}$ DOS reduction and the overall phonon hardening. Superfluid weight calculations show that conventional contributions dominate over quantum geometric effects due to the dispersive nature of bands near the Fermi level. This work demonstrates the effectiveness of integrating machine learning screening, first principles theory, and experimental synthesis for accelerating the discovery of new superconducting materials.

I. INTRODUCTION

During the century since superconductivity was discovered experimentally in Hg [1], serendipity has been the predominant way of finding new superconductors. Even after the theory of conventional superconductivity had been established by Bardeen, Cooper, and Schrieffer (BCS) [2], the new understanding of the role of electron-phonon correlations aided little in predicting novel superconducting materials and their critical parameters. New classes of superconductors, such as cuprates [3], pnictides [4], heavy fermion superconductors [5], organic superconductors [6], and very recently nickelates [7] or even the conventional superconductor MgB_2 [8], have been the result of accidental discoveries. One success of the theoretical prediction of superconductivity has been metallic hydrogen [9] and hydrides [10], which were conjectured to be the best candidates for high temperature superconductivity, based on the strong bonds and the light mass of hydrogen. Remarkably, hydrides currently hold the record for the highest experimentally observed superconducting critical temperatures [11], although at extremely high pressures. These materials were theoretically pre-

dicted using first-principles calculations before their experimental synthesis and characterization. The successful prediction and subsequent verification of superconductivity in these hydrogen-rich compounds represents a paradigm shift in materials discovery, demonstrating the power of computational methods to guide experimental efforts toward new superconductors.

Despite the success of first-principles theories in understanding the properties of superconducting materials, the immense vastness of the materials space and the high computational expense of these calculations impose a fundamental bottleneck for materials discovery. To address this challenge, machine learning (ML) has recently emerged as a powerful approach capable of accelerating the prediction of new superconductors [12–16]. ML models offer a means to rapidly screen candidate materials, which can then be strategically combined with conceptual guidelines derived from established theory, such as the identification of specific lattice motifs or structural features, for targeted searches. This ML-accelerated, theory-guided approach can be used to predict superconductivity in promising classes of materials, thereby guiding subsequent experimental synthesis and investigation.

In this context, materials with kagome lattices host quasi-flat bands with a large density of states, and have thus been a promising candidate for superconductivity. Flat bands with attractive interactions need

* These authors contributed equally.

† corresponding author: E. Morosan: emorosan@rice.edu

quantum geometry [17] to enable supercurrent in flat bands [18, 19], while with repulsive interactions, partially filled flat bands predominantly magnetize [20]. Recently, we conducted a comprehensive, ab initio investigation into the superconductivity of the flat-band kagome metal LaRu_3Si_2 [14]. Furthermore, we performed an ML-accelerated high-throughput screening of the entire 1:3:2 kagome family and identified several stable materials predicted to exhibit superconductivity.

Here, we report the first successful experimental confirmation of bulk superconductivity in one of these predicted systems: YRu_3B_2 . Furthermore, we report a second isostructural, new superconductor, LuRu_3B_2 . The Lu compound was initially overlooked in our high-throughput predictions [14] because its calculated phonon spectrum exhibits weakly imaginary modes, indicating a possible low-temperature dynamical instability.

Although the predicted critical temperatures (T_c) are higher (3.37 K for YRu_3B_2 and 1.88 K for LuRu_3B_2) than the experimental observations (0.81 K and 0.95 K, respectively), this result clearly demonstrates the merit of combining ML-driven screening with refined, post-screening ab initio calculations and experiments. This integrated approach provides a rigorous and efficient pathway from theoretical prediction to experimental realization of novel superconducting materials.

II. EXPERIMENTS

A. Methods

RRu_3B_2 ($R = \text{Y, Lu}$) samples were prepared from high-purity elements (Y 99.99%, Lu 99.99%, Ru 99.99%, and B 99.99%) in a stoichiometric composition 1:3:2. The elements were arc-melted on a water-cooled copper hearth in an argon atmosphere and remelted several times to ensure homogeneity. The mass loss during the melting process was negligible. The crystal structure was confirmed using powder X-ray diffraction in a Bruker D8 Advance diffractometer with $\text{Cu K}\alpha$ radiation. Rietveld refinements were performed using Highscore Plus.

Magnetization measurements $M(T;H)$ were performed in a QD Magnetic Property Measurement System (MPMS) equipped with the iQuantum Helium-3 option. Specific heat $C_p(T;H)$ measurements were performed in a Quantum Design (QD) Dynacool Physical Property Measurement System (PPMS) with a dilution refrigerator (DR) option.

B. Results and Discussion

RRu_3B_2 ($R = \text{Y, Lu}$) form in the CeCo_3B_2 -type structure, which crystallizes in the hexagonal $\text{P}6/\text{mmm}$ space group (# 191). In this structure, the Ru atoms arrange into a planar kagome network in the ab plane. The unit cell of RRu_3B_2 is shown in the inset of Fig. 1.

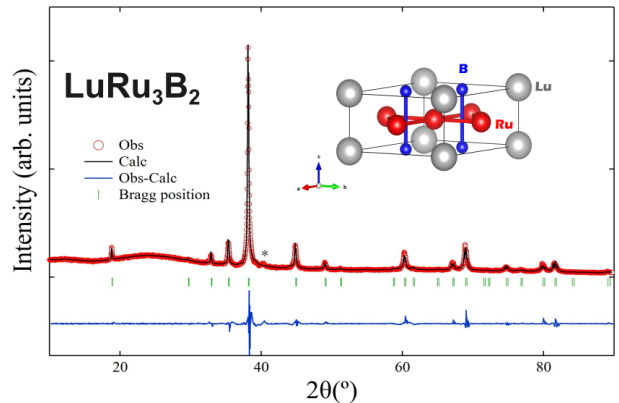


FIG. 1. Powder X-ray pattern for LuRu_3B_2 (red), with calculated pattern (black) and Bragg peak positions (green ticks) for space group $\text{P}6/\text{mmm}$. The asterisk denotes residual Ru. Inset: crystallographic unit cell of RRu_3B_2 .

Powder X-ray diffraction confirms the crystal structure and phase purity of the synthesized samples. The measured patterns (shown in Fig. 1 for LuRu_3B_2) can be fit to the expected CeCo_3B_2 structure, with the exception of a minute peak corresponding to elemental Ru, marked by an asterisk. Rietveld refinement of the patterns for the two compounds yields lattice parameters of $a = 5.475 \text{ \AA}$ and $c = 3.027 \text{ \AA}$ for YRu_3B_2 and $a = 5.448 \text{ \AA}$ and $c = 3.014 \text{ \AA}$ for LuRu_3B_2 .

We confirmed experimentally the superconductivity in YRu_3B_2 (black) and LuRu_3B_2 (blue) with thermodynamic measurements (Figs. 2-4). The measured susceptibility data $\chi = M/H$ was scaled by 4π and corrected for demagnetizing effects where $4\pi\chi_{\text{eff}} = 4\pi\chi/(1-N_d\chi)$. A demagnetizing factor $N_d = 1/3$ was used for a nearly spherical sample morphology, and the resulting superconducting fraction is close to 100% and 90% respectively in YRu_3B_2 and LuRu_3B_2 , confirming the bulk superconducting state in both compounds. For an applied field $H = 5 \text{ Oe}$, the critical temperatures, determined by the onset of diamagnetism in Fig. 2, are $T_c = 0.70 \text{ K}$ (YRu_3B_2) and 0.93 K (LuRu_3B_2). The lower critical field values can be estimated from the low temperature magnetization isotherms $M(H)$ ($T = 0.4 \text{ K}$) shown in Fig. 3. A linear fit of the low H magnetization suggests that the lower critical field H_{c1} , where $M(H)$ deviates from linearity (vertical arrow, inset), is close to 35 Oe and 48 Oe for YRu_3B_2 (black) and LuRu_3B_2 (blue) compounds, respectively. The determination of the upper critical field H_{c2} , defined by the field at which the $M(H)$ curve approaches zero, in YRu_3B_2 is impeded by a paramagnetic contribution (indicated by a finite slope in the $M(H)$ at high H), but it appears to be below 3000 Oe. For LuRu_3B_2 , the H_{c2} at $T = 0.4 \text{ K}$ is close to 700 Oe, and this is consistent with the findings from specific heat (discussed below).

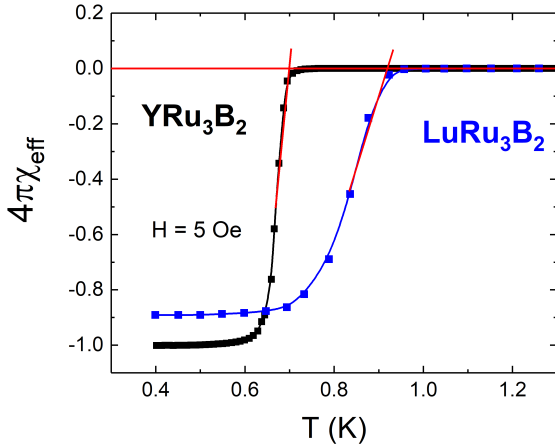


FIG. 2. Magnetic susceptibility $4\pi\chi_{eff}$ as a function of temperature for YRu_3B_2 (black) and $LuRu_3B_2$ (blue) at $H = 5$ Oe.

We were able to trace the superconducting state to lower temperatures and higher fields in specific heat (Fig. 4) measured down to $T = 60$ mK and applied magnetic field up to 800 Oe. A sharp jump was observed in the $H = 0$ specific heat at $T_c = 0.81$ K and 0.95 K, respectively, for YRu_3B_2 and $LuRu_3B_2$. Given that magnetic susceptibility was measured in a small applied field, the specific heat T_c values of $H = 0$ are slightly higher because, as expected, the increasing applied magnetic field suppresses T_c (fig. 4). The normal-state specific heat data for both samples can be modeled by the relation: $C_p/T = \gamma_n + \beta T^2$, where γ_n and β represent the electronic and phononic coefficients, respectively. The fitting parameters for $H = 0$ are determined as $\gamma_n = 15.1(1)$ mJ/molK², $\beta = 0.16(1)$ mJ/molK⁴ for the YRu_3B_2 sample, and $\gamma_n = 15.2(2)$ mJ/molK², $\beta = 0.48(1)$ mJ/molK⁴ for the $LuRu_3B_2$ sample. The superconducting electronic specific heat coefficient γ_e can be estimated using γ_n and the residual electronic specific heat coefficient γ_{res} , with the latter estimated from C_e/T at $T = 60$ mK and $H = 0$ (Fig. 4). Given that γ_{res} is much smaller than γ_n for both compounds, we approximate the electronic specific heat coefficient $\gamma_e = \gamma_n - \gamma_{res} \sim \gamma_n$ for both YRu_3B_2 and $LuRu_3B_2$.

The $H = 0$ entropy-conservation construct shown in Fig. 4(c, d) for YRu_3B_2 and $LuRu_3B_2$, respectively, produces similar values for the jump in the electronic specific heat C_e at T_c , $\Delta C_e/\gamma T_c \sim 1.1$ and 1.26. This value is close to, albeit slightly lower than the BCS predicted value of 1.43. This deviation can arise for a number of reasons, such as grain boundary effects (expected especially in polycrystalline samples) and non-BCS gap features, such as anisotropic or nodal superconducting gap. Our mean-field calculation based on a tight-binding model constructed from DFT band structure calculation gives pairing gaps non-uniform among the orbitals, as described in Section III D. An upturn in the C_e/T for

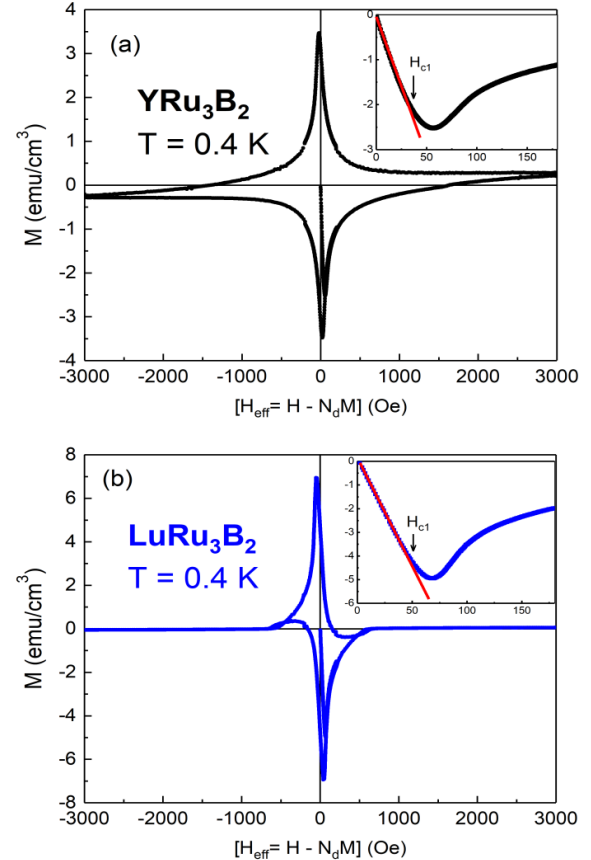


FIG. 3. Magnetization for (a) YRu_3B_2 (b) $LuRu_3B_2$ as a function of H_{eff} at $T = 0.4$ K, where $H_{eff} = H - N_d M$. Inset: linear fit of the low H magnetization showing where $M(H)$ deviates from linearity, giving an estimate for H_{c1} .

the Lu compound (Fig. 4d) is likely due to a nuclear Schottky anomaly at the low temperatures.

Using the experimental β values, along with the universal gas constant R , and considering $N = 6$ atoms per unit cell, the Debye temperature (θ_D) can be calculated as: $\theta_D = (12\pi^4 RN/5\beta)^{1/3}$. The Debye temperature turns out to be 283.7(3) K for YRu_3B_2 and 453(3) K for the $LuRu_3B_2$ compound. The electron-phonon coupling constant in these materials is determined using the following relation:

$$\lambda_{e-ph}^{exp} = \frac{1.04 + \mu^* \ln(\theta_D/1.45T_c)}{(1 - 0.62\mu^*) \ln(\theta_D/1.45T_c) - 1.04} \quad (1)$$

Here μ^* is the repulsive Coulomb interaction term, which is generally considered 0.13 for intermetallic samples. Substituting the values of θ_D and T_c yields $\lambda_{e-ph}^{exp} = 0.44$ (for YRu_3B_2) and 0.41 (for $LuRu_3B_2$), indicating the weakly coupled nature of superconductivity in both compounds. The electron-phonon coupling obtained from DFT calculations (Section III B) is $\lambda_{e-ph}^{th} = 0.477$ and

TABLE I. Summary of parameters describing YRu_3B_2 and LuRu_3B_2 properties.

| Compound | T_c (K) | H_{c1}, H_{c2} (Oe) | γ_n (mJ/molK ²) | β (mJ/molK ⁴) | $\Delta C_e/\gamma_n T_c$ | λ_{e-ph}^{exp} | m^* (m_e) | $\lambda_L^{exp}(0)$ (nm) | $\lambda_L^{th}(0)$ (nm) |
|---------------------------|--------------|--------------------------|---------------------------------------|------------------------------------|---------------------------|------------------------|--------------------|------------------------------|-----------------------------|
| YRu_3B_2 | 0.81 | 35, 730 | 15.1(1) | 0.16(1) | | 1.1 | 0.44 | 32.6(3) | 40(4) |
| LuRu_3B_2 | 0.95 | 48, 970 | 15.2(2) | 0.48(1) | | 1.26 | 0.41 | 32(1) | 35(3) |

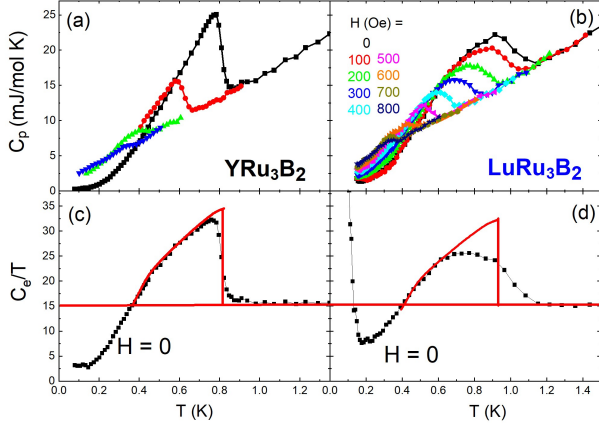


FIG. 4. $C_p(T)$ data for (a) YRu_3B_2 and (b) LuRu_3B_2 in applied fields ranging from 0–800 Oe. Electronic specific heat C_e scaled by temperature T for (c) YRu_3B_2 and (d) LuRu_3B_2 showing the entropy conservation construct.

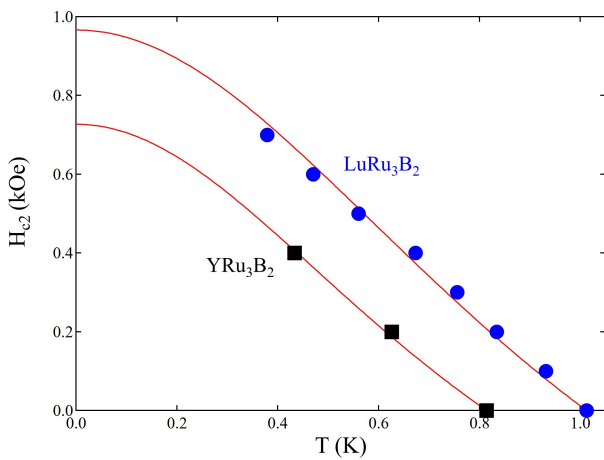


FIG. 5. $H_{c2}(T)$ phase diagram for YRu_3B_2 (black) and LuRu_3B_2 (blue), with the G-L fit (Eq. (2)) shown in red.

0.561 for the Y and Lu compounds, respectively, very close to the estimates from the experiment.

The Sommerfeld specific heat coefficient γ allows us to estimate the experimental London penetration depth $\lambda_L^{exp}(0)$: $\lambda_L(0) = (m^*/\mu_0 n e^2)^{1/2}$, where m^* is the electron effective mass scaled by the bare electron mass m_e , $m^*/m_e = (1 + \lambda_{e-ph}^{exp})$ and n is the carrier concentra-

tion. Due to the absence of single crystals which are required for Hall measurements and, therefore, experimental n estimates, we calculate the carrier concentration as $n = 3/V$ with V the unit cell volume determined experimentally from X-ray diffraction refinements. The value in the numerator here corresponds to the 3 electrons contributed by the trivalent ions Y^{3+} and Lu^{3+} in the two compounds. This yields $n = 3.82 \times 10^{-2} \text{ \AA}^{-3}$ and $3.87 \times 10^{-2} \text{ \AA}^{-3}$ for YRu_3B_2 and LuRu_3B_2 , respectively. The effective masses are $m^* = 1.44$ and $1.41 m_e$ for the Y and Lu compounds, respectively. Using these estimates, we can determine $\lambda_L^{exp}(0) = 32.6(3) \text{ nm}$ (Y) and $32(1) \text{ nm}$ (Lu). We have calculated the superfluid weight (superfluid stiffness) from DFT data (described in Section III E) and obtained the theoretical London penetration depth $\lambda_L^{th}(0) = 40(4) \text{ nm}$ (Y) and $35(3) \text{ nm}$ (Lu) in the xy-plane. The superconducting properties for YRu_3B_2 and LuRu_3B_2 compounds are summarized in Table I.

Fig. 5 shows the $H_{c2}(T)$ phase diagram for YRu_3B_2 (black) and LuRu_3B_2 (blue). The values of the critical fields H_{c2} are determined from C_p (T) data (symbols) and the fit to the Ginzburg-Landau equation [1] (red lines):

$$H_{c2}(T) = H_{c2}(0) \frac{1 - (T/T_c)^2}{1 + (T/T_c)^2} \quad (2)$$

These fits yield H_{c2} values close to 730 Oe and 970 Oe for YRu_3B_2 and LuRu_3B_2 , respectively.

In addition, the analysis in Section III E shows that, although quasi-flat bands exist in the band structure, the superfluid weight is mostly conventional; the geometric contribution is small because the dispersion of the bands at the Fermi level is large compared to the small superconducting order parameters for these low temperature superconductors.

III. THEORY

A. Methods

First-principles calculations were carried out within density functional theory (DFT) using the projector augmented-wave (PAW) method [21, 22], as implemented in the Vienna *ab initio* simulation package (VASP) [23, 24]. The exchange-correlation potential was treated within the generalized gradient approximation (GGA) using the Perdew-Burke-Ernzerhof (PBE) functional [25]. A plane-wave energy cutoff of 500 eV was used, and the Brillouin zone (BZ) was sampled with a Γ -centered

Monkhorst-Pack \mathbf{k} -point grid of $12 \times 12 \times 12$ [26]. Irreducible representations of the electronic states were obtained using IRVSP [27]. Maximally localized Wannier functions (MLWFs) were constructed for R - s , d , R - s , d , and B - s , p orbitals in local basis [28–32]. Based on these MLWFs, the Fermi surfaces, density of states, and orbital-resolved band structures were computed using WANNIERTOOLS [33].

Phonon spectra were calculated via the QUANTUM ESPRESSO package in the framework of density functional perturbation theory (DFPT). Electron-phonon coupling (EPC) properties were computed using the EPW package [34–37], included within QUANTUM ESPRESSO [38, 39]. Electron-phonon matrix elements were first computed on coarse \mathbf{k} -point and \mathbf{q} -point meshes ($8 \times 8 \times 12$ and $4 \times 4 \times 4$) and then interpolated onto finer grids ($32 \times 32 \times 32$) using maximally localized Wannier functions.

Superfluid-weight calculations were performed using the QUANTUM ESPRESSO package [40, 41], together with an in-house developed code (not publicly available). We employed the generalized gradient approximation (GGA) with the Perdew-Burke-Ernzerhof (PBE) exchange-correlation functional [42] revised for solids (PBEsol) [43], in combination with the scalar relativistic optimized norm-conserving Vanderbilt pseudopotentials (ONCVPPSP) from the PseudoDojo set [44]. We considered 25/11/16/3 valence electrons for Lu, Y, Ru, and B, respectively. Plane-wave energy cutoffs of 100 Ry for the wavefunctions and 1000 Ry for the density were chosen, along with a Methfessel-Paxton smearing [45] of 0.010 Ry. We computed the band-resolved superfluid weight with a $9 \times 9 \times 14$ self-consistent \mathbf{k} -point grid with 100 points along each path segment in the non-self-consistent calculation. The total superfluid weight required a non-self-consistent \mathbf{k} -point grid of $45 \times 45 \times 70$ for convergence.

B. Electronic band structure

To rationalize the suppression of T_c in $Y\text{Ru}_3\text{B}_2$, and LuRu_3B_2 compared with LaRu_3Si_2 from an electronic-structure perspective, we compare their band structures (see Fig. 6). As the lattice constants contract from La to Y and Lu (Table II), the bands become more dispersive, most notably the quasi-flat band near E_F from the Ru $d_{x^2-y^2}$ orbital (*i.e.*, the red bands in Fig. 6 on the $k_z = 0$ plane). In LaRu_3Si_2 , this quasi-flat band spans ~ 0.3 eV, whereas in $Y\text{Ru}_3\text{B}_2$ and LuRu_3B_2 its bandwidth increases to ~ 0.7 eV (Fig. 6). This broadening substantially reduces the DOS near E_F : the quasi-flat band contribution decreases from 1.589 states/eV/spin in LaRu_3Si_2 to 0.754 states/eV/spin in $Y\text{Ru}_3\text{B}_2$ and 0.753 states/eV/spin in LuRu_3B_2 , and the total DOS decreases from 5.308 states/eV/spin in La to 3.541 states/eV/spin in Y and 3.535 states/eV/spin in Lu. In contrast, the Ru d_{xz} DOS increases from 0.808 states/eV/spin in La to 1.125 states/eV/spin in Y

and 1.123 states/eV/spin in Lu (listed in Table II). Here all orbital labels refer to the local coordinate system defined in Refs. [14, 31, 32]. Since the EPC constant scales with the DOS as

$$\lambda = 2 \frac{D(\mu)}{N} \frac{\hbar \langle g^2 \rangle}{\hbar^2 \langle \omega^2 \rangle}, \quad (3)$$

where $\langle g^2 \rangle$ is the Fermi surface averaged EPC strength, N is the number of unit cell, $D(\mu)$ is the DOS at chemical potential μ , and $\langle \omega^2 \rangle$ the McMillan average phonon frequency. The reduced $D(\mu)$ directly weakens EPC strength in $Y\text{Ru}_3\text{B}_2$ and LuRu_3B_2 . This trend is consistent with recent experimental results on $Y\text{Ru}_3\text{Si}_2$ [46], where replacing La by the smaller Y ion reduces the in-plane lattice constant a from 5.715 Å to 5.472 Å and T_c from 6.8 K to 3.4 K. Orbital-resolved band analysis further shows that, in $RR\text{Ru}_3\text{B}_2$ ($R = Y, \text{Lu}$), the Ru $d_{x^2-y^2}$ -derived quasi-flat band does not show an effective hole doping relative to LaRu_3Si_2 . Instead, the Ru d_{xz} and d_{z^2} bands shift upward and become hole-doped (Fig. 6). Moreover, the d_{z^2} -derived band lies substantially higher in energy (green bands in Fig. 6), which weakens the d_{z^2} -bonding-driven structural instability toward the $Cccm$ (orthorhombically distorted) phase [47].

TABLE II. Lattice constants (in unit of Å) after full relaxation, total (and orbital-projected) DOS at the Fermi level (in unit of states/eV/spin), and electron-phonon coupling constant λ_{e-ph} for $Y\text{Ru}_3\text{B}_2$, LuRu_3B_2 , and LaRu_3Si_2 .

| | $Y\text{Ru}_3\text{B}_2$ | LuRu_3B_2 | LaRu_3Si_2 |
|-----------------------|--------------------------|---------------------------|----------------------------|
| a | 5.5037 | 5.4762 | 5.7154 |
| c | 3.0267 | 3.0144 | 3.5755 |
| $D(E_F)$ (total) | 3.535 | 3.541 | 5.308 |
| $D(E_F)(d_{x^2-y^2})$ | 0.754 | 0.753 | 1.589 |
| $D(E_F)(d_{xz})$ | 1.125 | 1.123 | 0.808 |
| λ_{e-ph} | 0.477 | 0.561 | 0.831 |

C. Phonons and electron-phonon coupling

To assess phononic effects in $RR\text{Ru}_3\text{B}_2$ ($R = Y, \text{Lu}$) and benchmark against LaRu_3Si_2 , we compute phonon dispersions within DFPT and analyze their mode character and contribution to the electron-phonon coupling (EPC). Relative to LaRu_3Si_2 , the phonon spectra of $RR\text{Ru}_3\text{B}_2$ (see Fig. 7) are overall shifted to higher energies, consistent with the smaller atomic mass of B with respect to Si, the smaller lattice constants, and stiffer effective force constants. This increases the characteristic phonon scale $\langle \omega^2 \rangle$ and therefore tends to reduce the EPC constant λ for comparable $\langle g^2 \rangle$, particularly for the coupling between Ru $d_{x^2-y^2}$ states and Ru in-plane x modes.

In LuRu_3B_2 , we additionally identify a low-frequency branch at Γ dominated by Lu in-plane (xy) motion that becomes soft (see Fig. 7). The corresponding two-dimensional mode transforms as Γ_6^- and is compatible

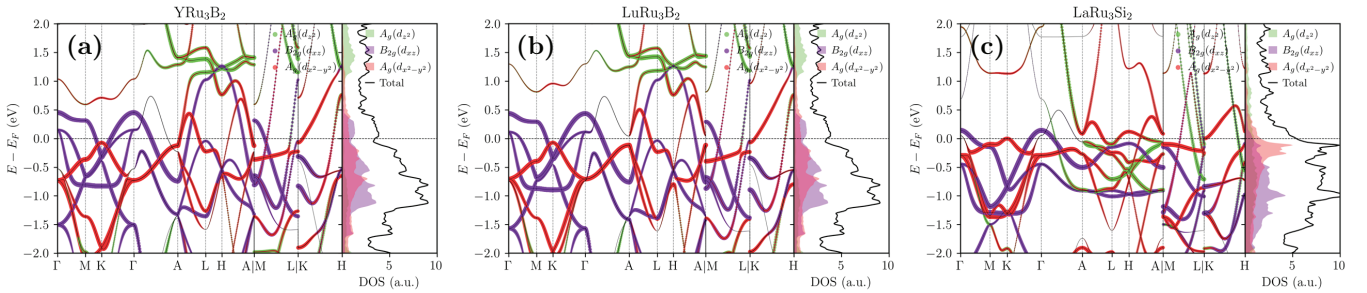


FIG. 6. Orbital-projected band structure and density of states (DOS) of the $P6/mmm$ structure for (a) YRu_3B_2 , (b) LuRu_3B_2 , and (c) LaRu_3Si_2 . The d orbitals (specifically d_{z^2} , $d_{x^2-y^2}$, and d_{xz}) of Ru atoms are projected onto the band structure, with the radius of the circles proportional to the projected weight.

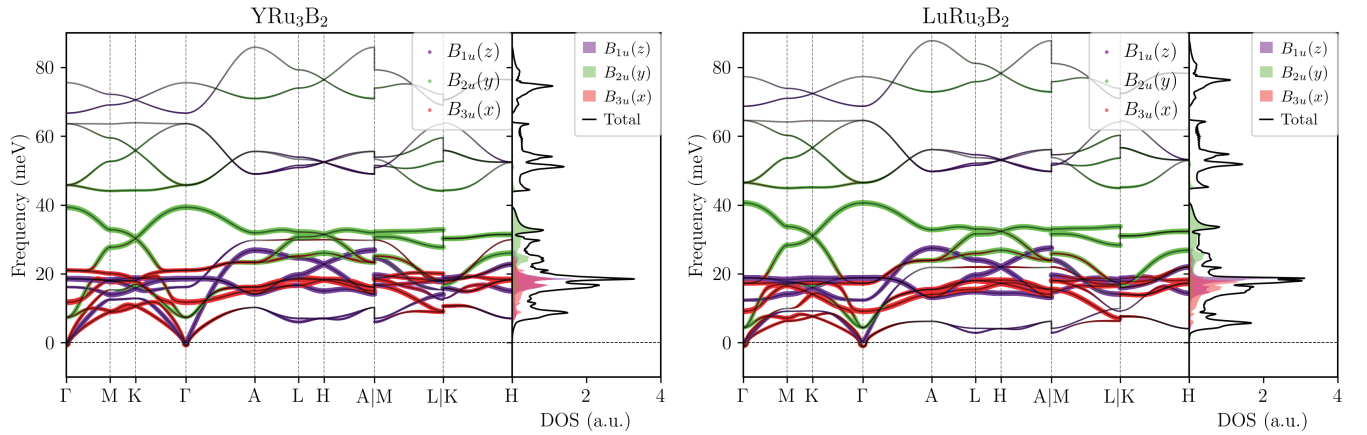


FIG. 7. Mode-projected phonon band structure and density of states (DOS) of the $P6/mmm$ structure for YRu_3B_2 (left panel) and LuRu_3B_2 (right panel). The phonon modes (defined in local coordinates) of Ru atoms are projected onto the phonon band structure, with the radius of the circles proportional to the projected weight.

with a symmetry lowering to $Amm2$ (No. 38) (the representation follows the convention on the *Bilbao Crystallographic Server* [48–50]), *i.e.*, a possible C_3 -breaking distortion at low temperature. To avoid an artificial enhancement of λ associated with an incipient instability within harmonic EPC theory, we evaluate EPC using the stable phonon spectrum obtained at relatively larger electronic smearing, yielding $\lambda \simeq 0.561$ (Fig. 8) and an estimated $T_c \simeq 3.27$ K from the Allen–Dynes modified McMillan equation [51–53] with $\mu^* = 0.1$ for LuRu_3B_2 . For YRu_3B_2 , we obtain $\lambda \simeq 0.477$ and $T_c \simeq 1.88$ K. For reference, the $T_c \simeq 6.8$ K reported in Ref. [14] was obtained using coarser \mathbf{k} and \mathbf{q} -point meshes in a high-throughput workflow. The theoretical values of λ with increased value for the smearing are close to the estimates based on experiments, namely $\lambda_{e-ph}^{exp} = 0.44$ (for YRu_3B_2) and 0.41 (for LuRu_3B_2) (see Table I in Results and Discussion.). It is worth noting that matching the experimental T_c within the Allen–Dynes framework requires $\mu^* \approx 0.14$ for Y and $\mu^* \approx 0.17$ for Lu. The mode-projected phonon DOS and the phonon dispersions in Fig. 7 show that the Ru in-plane x mode lies systematically below the corresponding y modes, mirroring the

trend in LaRu_3Si_2 . As we show below and in Fig. 8, this low-frequency Ru- x branch provides the dominant contribution to λ .

To quantify the microscopic EPC, we project the *ab initio* EPC tensor into a Wannier basis using EPW [34–37]. The leading real-space EPC matrix elements between Ru $d_{x^2-y^2}$ electrons and Ru x phonons are essentially the same for both YRu_3B_2 (0.02024 Ry/Bohr), LuRu_3B_2 (0.02073 Ry/Bohr) and LaRu_3Si_2 (0.02043 Ry/Bohr). Given that the DOS at E_F from Ru d_{xz} and $d_{x^2-y^2}$ orbitals is comparable (Table II), we also evaluate the corresponding EPC elements for Ru d_{xz} electrons coupled to Ru x phonons, obtaining 0.01254 (Y), 0.01231 (Lu), and 0.00925 (La). With a matrix element roughly half as large and similar DOS, Eq. (3) implies that the d_{xz} channel contributes at the level of $\sim 1/4$ of the $d_{x^2-y^2}$ channel, leaving the $d_{x^2-y^2}$ states as the dominant contributor to the total λ as in LaRu_3Si_2 [14]. Taken together, the near invariance of these real-space EPCs indicates that the reduced λ in RRu_3B_2 originates from the suppressed $d_{x^2-y^2}$ DOS and the overall hardening of the phonon spectrum.

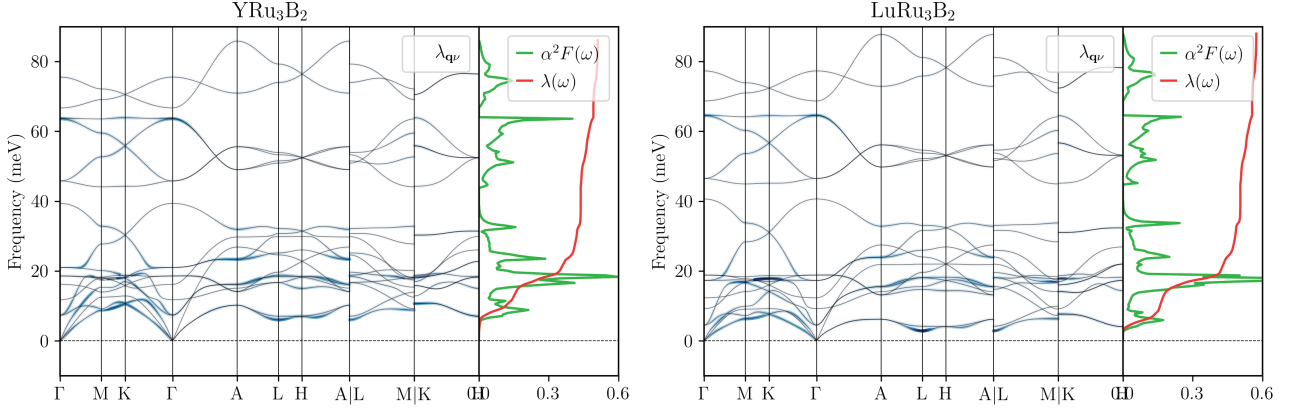


FIG. 8. Phonon band structure, Eliashberg spectral function $\alpha^2 F(\omega)$, and electron-phonon coupling constant $\lambda(\omega)$ for YRu_3B_2 (left) and LuRu_3B_2 (right).

D. Mean-field tight-binding model analysis of the superconducting order parameter structure

We construct a tight-binding model from DFT by generating Wannier functions for the two kagome compounds. Using this model, we perform self-consistent mean-field superconductivity calculations following the approach described in Ref. [14], with an on-site attractive interaction applied uniformly to each orbital. This calculation yields superconducting order parameters for all 32 orbitals, revealing the relative contribution of different atoms and orbitals to superconductivity. The interaction strength is chosen to produce superconducting gaps consistent with the experimental T_c . We verified that the qualitative trends described below remain robust across a range of interaction values.

In both YRu_3B_2 and LuRu_3B_2 , we find that the three d_{xz} orbitals of Ru have the same and the largest order parameter. Of the other contributions, the Ru $d_{x^2-y^2}$, d_{yz} , and d_{xy} orbitals (three each) are within the same order of magnitude as the Ru d_{xz} one. The contributions from the remaining Ru orbitals (s and d_{z^2}), and all Lu and B orbitals, are one or more orders of magnitude smaller. Superconductivity is thus primarily caused by pairing related to the orbitals of the Ru atoms that form the kagome structure. Here, it is interesting to note that DFT analysis of superconductivity for LaRu_3Si_2 found the Ru $d_{x^2-y^2}$ orbital to also dominate the superconducting order parameter [14]. However, the orbital content of the pairing gap differs because of the dominant density of states from $d_{x^2-y^2}$ close to Fermi level in LaRu_3Si_2 , while in YRu_3B_2 and LuRu_3B_2 the d_{xz} and $d_{x^2-y^2}$ contribute similarly to the density of states, as shown in Fig. 6. Our mean-field description reflects mainly the density of states, as the interaction is assumed uniform for all orbitals; for a more refined calculation, the orbital-dependence of interactions as well as possible nearest-neighbor interactions would be needed.

E. Superfluid weight and penetration depth calculations

We calculate the superfluid weight (superfluid stiffness) tensor $D_s = D_{geom} + D_{conv}$, including both the conventional contribution D_{conv} , proportional to the band dispersion, and the geometric one D_{geom} , arising from the quantum geometry of the bands [18, 54]. To simplify the computations, we utilize the zero-temperature formula for the superfluid weight which assumes uniform pairing [55] (i, j are the Cartesian coordinates x, y, z):

$$D_{conv}^{ij} = \frac{1}{V} \sum_{km} \frac{\Delta^2}{\sqrt{\epsilon_m^2 + \Delta^2}} \partial_i \epsilon_m \partial_j \epsilon_m \quad (4)$$

$$D_{geom}^{ij} = \frac{1}{V} \sum_{k, m, n \neq m} \frac{\epsilon_n - \epsilon_m}{\epsilon_m + \epsilon_n} \left[\frac{\Delta^2}{\sqrt{\epsilon_m^2 + \Delta^2}} - \frac{\Delta^2}{\sqrt{\epsilon_n^2 + \Delta^2}} \right] \times (\langle \partial_i m | n \rangle \langle n | \partial_j m \rangle + \text{H.c.}) \quad (5)$$

Here ϵ_m is the energy dispersion shifted by the Fermi level, and it is a function of momentum \mathbf{k} with m as the band index. The energy dispersions as well as the Bloch functions $|m\rangle$ and their derivatives are obtained by DFT. The superconducting gap is set to 2 meV.

Our calculations reveal that the superfluid weight in these compounds is dominated by the conventional contribution. This is expected given the dispersive nature of bands near the Fermi level and that quantum geometric contributions become significant only when the pairing gap is comparable to or exceeds the bandwidth, which is not the case here. Note that the gap value used, 2 meV, is larger than what could be estimated from the experimental T_c via the BCS relation $\Delta \simeq 1.76T_c$ (which gives $\Delta = 0.106$ meV for the Y and 0.147 meV for the Lu compound), but we have checked that the calculation gives a good estimate for the conventional contribution since it does not depend strongly on the gap. The geometric contribution is overestimated, which however does not change the conclusion that the conventional one domi-

nates. The values for the superfluid weight components are summarized in Table III.

To gain insight into which parts of the band structure contribute to the superfluid weight the most, we investigate the superfluid weight integrand $D_s^{ij}(\mathbf{k}, m)$ when the total superfluid weight is $D_s^{ij} = \sum_{\mathbf{k}, m} D_s^{ij}(\mathbf{k}, m)$, see Equations (4)-(5). Figure 9 shows the diagonal components of the superfluid weight integrand. The largest contributions for the xx and yy of the superfluid-weight integrand components are found along the $\Gamma - M - K - \Gamma$ and $A - L - H - A$ lines, while the zz component vanishes on these planes. Conversely, D_{conv}^{zz} is non-zero only along the $\Gamma - A$, $M - L$ and $K - H$ lines, where D_{conv}^{xx} and D_{conv}^{yy} vanish. This anisotropy follows from symmetry constraints and the fact that D_{conv} is directly proportional to the band dispersion. The crystal belongs to space group $P6/mmm$ (No. 191), which contains mirror planes perpendicular to k_x , k_y , and k_z passing through Γ , as well as mirror planes containing the $A - L - H$ and $K - M - L - H$ paths set by the translational symmetries. These mirror symmetries force the component of the band dispersion normal to a mirror plane to vanish at mirror-invariant points. Thus, the dispersion along k_z is forbidden in $\Gamma - M - K$ and $A - L - H$ planes, while the $k_{x,y}$ one is suppressed along $\Gamma - A$, $M - L$ and $K - H$ lines. To be precise, along the $H - K$ line, only the xx component is forced to be zero by symmetry arguments. However, the zero dispersion along this direction, together with the other two non-dispersive directions related by the C_{3z} symmetry, hinders the possibility of a large yy dispersion, as shown in Figure 9.

The London penetration depth λ_L is related to the superfluid weight by

$$\lambda_L = (\mu_0 D_s)^{-1/2}. \quad (6)$$

We use this formula with D_s^{ii} to give the penetration depths, λ_z^{th} in the $i = z$ direction, and λ_{xy}^{th} in the $i = x, y$ directions which are nearly identical due to the approximate xy -isotropies of the system (see Figure 10), even when the system is not xy -symmetric. The penetration depth predictions are summarized in Table I. The calculations show that YRu_3B_2 has slightly larger penetration depths than LuRu_3B_2 , however the error range partially overlaps. Both show a larger penetration depth in the xy -plane compared to the z direction.

IV. CONCLUSIONS

We discovered two new superconductors, YRu_3B_2 and LuRu_3B_2 , both predicted through ML-accelerated high-throughput screening of kagome lattice materials. These compounds crystallize in the hexagonal CeCo_3B_2 -type structure with planar Ru kagome networks, and exhibit bulk superconductivity confirmed through magnetization, specific heat, and resistivity measurements with superconducting volume fractions close to 100%.

The experimental realization of these materials validates the predictive power of combining ML with first-principles calculations for superconductor discovery, even though the observed critical temperatures are lower than initially predicted. Our theoretical analysis explains this discrepancy through the incipient phase transition leading to an excessive softening of phonon modes in the calculations.

The contraction of lattice parameters from LaRu_3Si_2 to the smaller Y and Lu analogs increases band dispersion, particularly for the quasi-flat kagome band derived from Ru $d_{x^2-y^2}$ orbitals. This enhanced dispersion reduces the density of states near the Fermi level, directly weakening the electron-phonon coupling constant and consequently suppressing T_c . Detailed phonon and Wannier-resolved EPC analysis shows that the dominant coupling channel remains the Ru $d_{x^2-y^2}$ states interacting with the low-frequency in-plane Ru- x branch, and its leading real-space matrix elements are nearly unchanged across the three compounds. On the other hand, our mean-field analysis shows that, assuming uniform interaction for all orbitals, YRu_3B_2 and LuRu_3B_2 have comparable contributions from both d_{xz} and $d_{x^2-y^2}$ orbitals due to their similar densities of states near the Fermi level. This shift in orbital character reflects the band structure reorganization accompanying lattice contraction, with d_{xz} and d_{z^2} bands becoming hole-doped while the $d_{x^2-y^2}$ band remains near its original filling.

Our superfluid weight calculations demonstrate that conventional contributions dominate over quantum geometric effects in these materials. This is expected as quantum geometric contributions become significant only when the pairing gap is comparable to or exceeds the bandwidth, a condition not met in YRu_3B_2 and LuRu_3B_2 . The calculated London penetration depths show moderate anisotropy between in-plane and out-of-plane directions, reflecting the quasi-two-dimensional character of the kagome structure.

The successful prediction-to-realization pipeline demonstrated here, from ML screening through first principles calculations to experimental synthesis and characterization, represents a significant advance in accelerating superconductor discovery. While the materials space of the 1:3:2 kagome family is manageable with current computational methods, this integrated approach becomes increasingly valuable when extended to larger materials spaces where exhaustive first-principles calculations are prohibitively expensive. The key is the strategic combination of rapid ML-based pre-screening to identify promising candidates, followed by targeted high-accuracy calculations and experimental investigation of the most viable predictions.

The broader significance of this work extends beyond these specific compounds. It provides a demonstration that the century-old paradigm of serendipitous superconductor discovery can be complemented, and in some cases replaced, by systematic, computation-guided materials design. As ML models improve and computational

TABLE III. Overview of total superfluid weight components computed from DFT data of YRu_3B_2 and LuRu_3B_2 with the uniform pairing assumption, and London penetration depths obtained from them. The calculation was done with $\Delta = 2$ meV.

| Compound | xy λ_L^{th} (nm) | z λ_L^{th} (nm) | D_s^{xx} (1/Hm) | D_s^{yy} (1/Hm) | D_s^{zz} (1/Hm) | D_{conv}^{xx} (1/Hm) | D_{conv}^{yy} (1/Hm) | D_{conv}^{zz} (1/Hm) | D_{geom}^{xx} (1/Hm) | D_{geom}^{yy} (1/Hm) | D_{geom}^{zz} (1/Hm) |
|---------------------------|-----------------------------|----------------------------|----------------------|----------------------|----------------------|---------------------------|---------------------------|---------------------------|---------------------------|---------------------------|---------------------------|
| YRu_3B_2 | 40 ± 4 | 25 ± 9 | $5.1 \cdot 10^{20}$ | $5.1 \cdot 10^{20}$ | $1.3 \cdot 10^{21}$ | $5.1 \cdot 10^{20}$ | $5.1 \cdot 10^{20}$ | $1.3 \cdot 10^{21}$ | $9.3 \cdot 10^{17}$ | $9.3 \cdot 10^{17}$ | $3.4 \cdot 10^{18}$ |
| LuRu_3B_2 | 35 ± 3 | 21 ± 11 | $6.4 \cdot 10^{20}$ | $6.4 \cdot 10^{20}$ | $1.7 \cdot 10^{21}$ | $6.4 \cdot 10^{20}$ | $6.4 \cdot 10^{20}$ | $1.7 \cdot 10^{21}$ | $7.0 \cdot 10^{17}$ | $7.0 \cdot 10^{17}$ | $1.3 \cdot 10^{18}$ |

resources expand, this approach will become increasingly powerful for navigating the vast materials space and identifying superconductors with tailored properties. The successful realization of YRu_3B_2 and LuRu_3B_2 is a step toward this future, where theory, computation, and experiment work in concert to accelerate the discovery and characterization of quantum materials.

ACKNOWLEDGMENTS

This work was supported by a collaboration between The Kavli Foundation, Klaus Tschira Stiftung, and

Kevin Wells, and by the Jane and Aatos Erkko Foundation, the Keele Foundation and the Magnus Ehrnrooth Foundation, as part of the SuperC collaboration. B.A.B., M.A.L.M., and P.T. were supported by a grant from the Simons Foundation (SFI-MPS-NFS-00006741-01, B.A.B.; SFI-MPS-NFS-00006741-13, M.A.L.M.; SFI-MPS-NFS-00006741-12, P.T.) in the Simons Collaboration on New Frontiers in Superconductivity. We thank Kristjan Haule and Théo Cavignac for useful discussions.

Note added—While preparing this manuscript, two works appeared on arxiv.org that report experimental observation of the YRu_3B_2 superconductor [56, 57].

[1] M. Tinkham, *Introduction to Superconductivity*, McGraw-Hill, 2nd Edition (1996).

[2] J. Bardeen, L. N. Cooper, and J. R. Schrieffer, Theory of superconductivity, *Phys. Rev.* **108**, 1175 (1957).

[3] J. G. Bednorz and K. A. Müller, Possible high T_c superconductivity in the Ba-La-Cu-O system, *Zeitschrift für Physik B Condensed Matter* **64**, 189 (1986).

[4] Y. Kamihara, T. Watanabe, M. Hirano, and H. Hosono, Iron-based layered superconductor $\text{La}[\text{O}_{1-x}\text{F}_x]\text{FeAs}$ ($x = 0.05\text{--}0.12$) with $T_c = 26$ K, *Journal of the American Chemical Society* **130**, 3296 (2008), <https://doi.org/10.1021/ja800073m>.

[5] F. Steglich, J. Aarts, C. D. Bredl, W. Lieke, D. Meschede, W. Franz, and H. Schäfer, Superconductivity in the presence of strong pauli paramagnetism: CeCu_2Si_2 , *Phys. Rev. Lett.* **43**, 1892 (1979).

[6] M. R. D. Jérôme, A. Mazaud and K. Bechgaard, Superconductivity in a synthetic organic conductor (TMTSF)2PF 6, *J. Physique Lett.* **41**, 4 (1980).

[7] D. Li, K. Lee, B. Y. Wang, M. Osada, S. Crossley, H. R. Lee, Y. Cui, Y. Hikita, and H. Y. Hwang, Superconductivity in an infinite-layer nickelate, *Nature* **572**, 624–627 (2019), <https://doi.org/10.1038/s41586-019-1496-5>.

[8] D. Li, K. Lee, B. Y. Wang, M. Osada, S. Crossley, H. R. Lee, Y. Cui, Y. Hikita, and H. Y. Hwang, Superconductivity at 39 K in magnesium diboride., *Nature* **410**, 63–64 (2001), <https://doi.org/10.1038/35065039>.

[9] N. W. Ashcroft, Metallic Hydrogen:A High-Temperature Superconductor?, *Phys. Rev. Lett.* **21**, 1748 (1968).

[10] N. W. Ashcroft, Hydrogen Dominant Metallic Alloys: High Temperature Superconductors?, *Phys. Rev. Lett.* **92**, 187002 (2004).

[11] L. Boeri, R. G. Hennig, P. J. Hirschfeld, G. Profeta, A. Sanna, E. Zurek, W. E. Pickett, M. Amsler, R. Dias, M. Eremets, C. Heil, R. Hemley, H. Liu, Y. Ma, C. Pierleoni, A. Kolmogorov, N. Rybin, D. Novoselov, V. I. Anisimov, A. R. Oganov, C. J. Pickard, T. Bi, R. Arita, I. Errea, C. Pellegrini, R. Requist, E. Gross, E. R. Margine, S. R. Xie, Y. Quan, A. Hire, L. Fanfarillo, G. R. Stewart, J. J. Hamlin, V. Stanev, R. S. Gonnelli, E. Piatti, D. Romanin, D. Daghero, and R. Valentini, The 2021 room-temperature superconductivity roadmap, *J. Phys.: Condens. Matter* **34**, 183002 (2022).

[12] K. Gao, T. Cerqueira, A. Sanna, Y.-W. Fang, Đorđe. Dangić, I. Errea, H.-C. Wang, S. Botti, and M. A. L. Marques, The maximum T_c of conventional superconductors at ambient pressure, *Nat Commun* **16**, 8253 (2025).

[13] J. B. Gibson, A. C. Hire, P. Prakash, P. M. Dee, B. Geisler, J. S. Kim, Z. Li, J. J. Hamlin, G. R. Stewart, P. J. Hirschfeld, and R. G. Hennig, Developing a Complete AI-Accelerated Workflow for Superconductor Discovery, *arXiv:2503.20005* <https://doi.org/10.48550/arXiv.2503.20005> (2025).

[14] J. Deng, Y. Jiang, T. F. T. Cerqueira, H. Hu, E. O. Lamponen, D. Călugăru, Z. W. Hanqi Pi, M. G. Vergniory, E. Morosan, T. Neupert, S. Blanco-Canosa, C. Felser, K. Haule, M. A. L. Marques, P. Törmä, and B. A. Bernevig, Theory of Superconductivity in LaRu_3Si_2 and Predictions of New Kagome Flat Band Superconductors, *arXiv:2503.20867* <https://doi.org/10.48550/arXiv.2503.20867> (2025).

[15] P. Prakash, J. B. Gibson, Z. Li, G. D. Gianluca, J. Esquivel, E. Fuemmeler, B. Geisler, J. S. Kim, A. Roitberg, E. B. Tadmor, M. Liu, S. Martiniani, G. R. Stewart, J. J. Hamlin, P. J. Hirschfeld, and R. G. Hennig, Guided Diffusion for the Discovery of New Superconductors, *arXiv:2509.25186* <https://doi.org/10.48550/arXiv.2509.25186> (2025).

[16] O. Lesser, Y. Liu, N. Maus, A. Panigrahi, K. Mal-

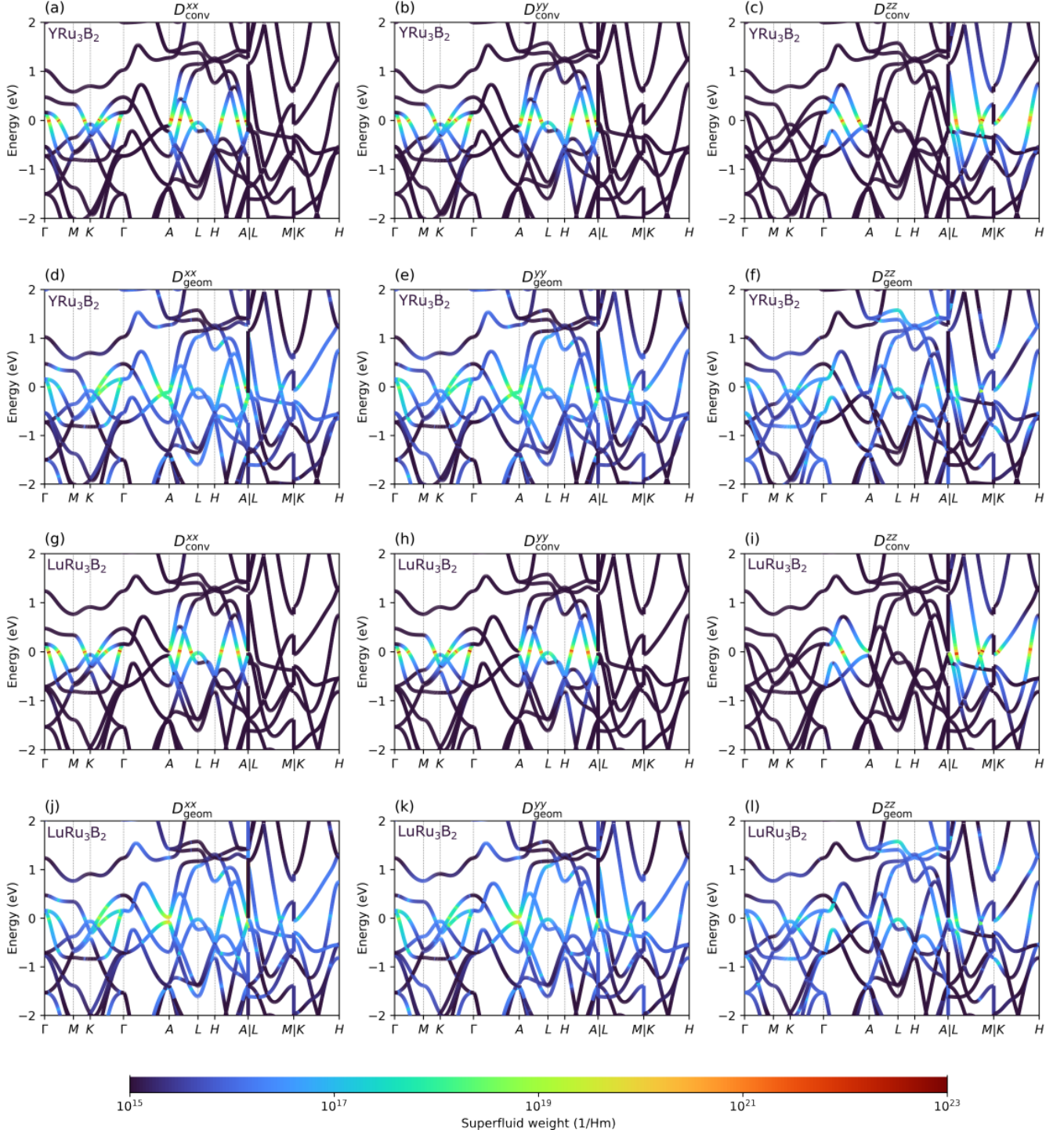


FIG. 9. Integrands $D^{ij}(\mathbf{k}, m)$ of the superfluid weight tensor components for YRu_3B_2 in the first two rows and LuRu_3B_2 in the last two, calculated using Equations (4)-(5) and DFT data. The conventional contribution is larger and concentrated on the Fermi energy while the geometric is smaller and more spread out. Note that the colorscale is logarithmic.

layya, L. M. Schoop, J. R. Gardner, and E.-A. Kim, Learning to predict superconductivity, arXiv:2510.07373 <https://doi.org/10.48550/arXiv.2510.07373> (2025).

[17] J. Yu, B. A. Bernevig, R. Queiroz, E. Rossi, P. Törmä, and B.-J. Yang, Quantum geometry in quantum materi-

als, npj Quantum Materials **10**, 101 (2025).
 [18] S. Peotta and P. Törmä, Superfluidity in topologically nontrivial flat bands, Nat Commun **6**, 8944 (2015).
 [19] P. Törmä, S. Peotta, and B. A. Bernevig, Superconductivity, superfluidity and quantum geometry in twisted

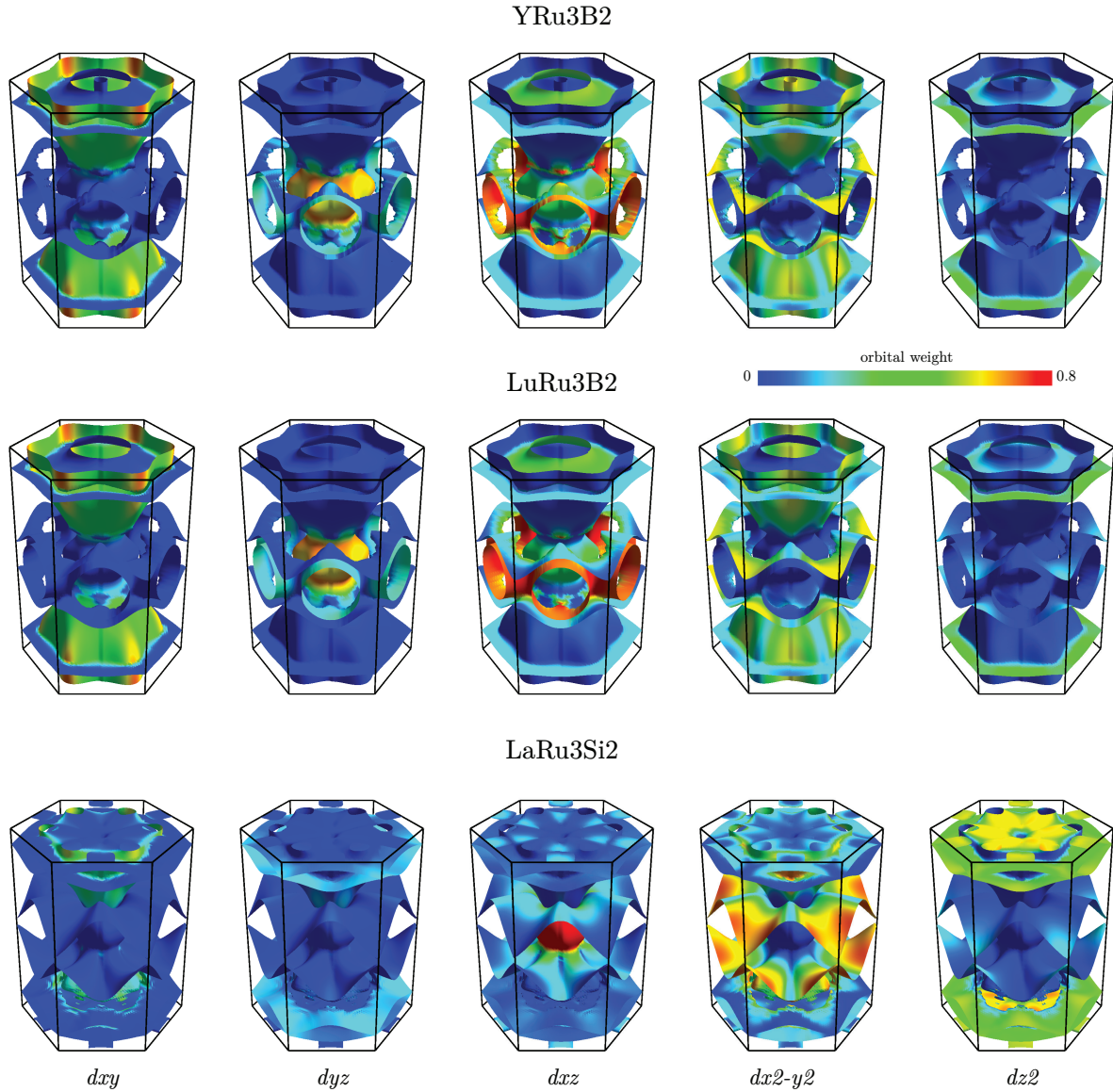


FIG. 10. Orbital-resolved Fermi surfaces of YRu_3B_2 , LuRu_3B_2 , and LaRu_3Si_2 in $P6/mmm$ phase, with the color denoting the orbital weight of Ru d orbitals in local coordinate.

multilayer systems, *Nat Rev Phys* **4**, 528 (2022).

[20] H. Hu, O. Vafek, K. Haule, and B. A. Bernevig, Ferromagnetism vs. Antiferromagnetism in Narrow-Band Systems: Competition Between Quantum Geometry and Band Dispersion (2025), arXiv:2509.03575 [cond-mat.str-el].

[21] P. E. Blöchl, Projector augmented-wave method, *Phys. Rev. B* **50**, 17953 (1994).

[22] G. Kresse and D. Joubert, From ultrasoft pseudopotentials to the projector augmented-wave method, *Phys. Rev. B* **59**, 1758 (1999).

[23] G. Kresse and J. Furthmüller, Efficiency of ab-initio total energy calculations for metals and semiconductors using a plane-wave basis set, *Computational Materials Science* **6**, 15 (1996).

[24] G. Kresse and J. Furthmüller, Efficient iterative schemes for ab initio total-energy calculations using a plane-wave basis set, *Phys. Rev. B* **54**, 11169 (1996).

[25] J. P. Perdew, K. Burke, and M. Ernzerhof, Generalized Gradient Approximation Made Simple, *Phys. Rev. Lett.* **77**, 3865 (1996).

[26] H. J. Monkhorst and J. D. Pack, Special points for brillouin-zone integrations, *Phys. Rev. B* **13**, 5188 (1976).

[27] J. Gao, Q. Wu, C. Persson, and Z. Wang, Irvsp : To obtain irreducible representations of electronic states in the VASP, *Computer Physics Communications* **261**, 107760 (2021).

[28] A. A. Mostofi, J. R. Yates, Y.-S. Lee, I. Souza, D. Vanderbilt, and N. Marzari, Wannier90 : A tool for obtaining maximally-localised Wannier functions, *Computer Physics Communications* **178**, 685 (2008).

[29] A. A. Mostofi, J. R. Yates, G. Pizzi, Y.-S. Lee, I. Souza, D. Vanderbilt, and N. Marzari, An updated version of Wannier90: A tool for obtaining maximally-localised Wannier functions, *Computer Physics Communications* **185**, 2309 (2014).

[30] G. Pizzi, V. Vitale, R. Arita, S. Blügel, F. Freimuth, G. Géranton, M. Gibertini, D. Gresch, C. Johnson, T. Koretsune, J. Ibañez-Azpiroz, H. Lee, J.-M. Lihm, D. Marchand, A. Marrazzo, Y. Mokrousov, J. I. Mustafa, Y. Nohara, Y. Nomura, L. Paulatto, S. Poncé, T. Ponweiser, J. Qiao, F. Thöle, S. S. Tsirkin, M. Wierzbowska, N. Marzari, D. Vanderbilt, I. Souza, A. A. Mostofi, and J. R. Yates, Wannier90 as a community code: new features and applications, *Journal of Physics: Condensed Matter* **32**, 165902 (2020).

[31] J. Deng, R. Zhang, Y. Xie, X. Wu, and Z. Wang, Two elementary band representation model, Fermi surface nesting, and surface topological superconductivity in AV_3Sb_5 ($A = K, Rb, Cs$), *Phys. Rev. B* **108**, 115123 (2023).

[32] Y. Jiang, H. Hu, D. Călugăru, C. Felser, S. Blanco-Canosa, H. Weng, Y. Xu, and B. A. Bernevig, FeGe as a building block for the kagome 1:1, 1:6:6, and 1:3:5 families: Hidden d -orbital decoupling of flat band sectors, effective models, and interaction Hamiltonians, *Phys. Rev. B* **111**, 125163 (2025).

[33] Q. Wu, S. Zhang, H.-F. Song, M. Troyer, and A. A. Soluyanov, WannierTools : An open-source software package for novel topological materials, *Computer Physics Communications* **224**, 405 (2018).

[34] F. Giustino, M. L. Cohen, and S. G. Louie, Electron-phonon interaction using wannier functions, *Phys. Rev. B* **76**, 165108 (2007).

[35] J. Noffsinger, F. Giustino, B. D. Malone, C.-H. Park, S. G. Louie, and M. L. Cohen, EPW: A program for calculating the electron-phonon coupling using maximally localized Wannier functions, *Computer Physics Communications* **181**, 2140 (2010).

[36] S. Poncé, E. R. Margine, C. Verdi, and F. Giustino, EPW: Electron-phonon coupling, transport and superconducting properties using maximally localized Wannier functions, *Computer Physics Communications* **209**, 116 (2016), arXiv:1604.03525 [cond-mat].

[37] H. Lee, S. Poncé, K. Bushick, S. Hajinazar, J. Lafuente-Bartolome, J. Leveillee, C. Lian, J.-M. Lihm, F. Macheda, H. Mori, H. Paudyal, W. H. Sio, S. Tiwari, M. Zacharias, X. Zhang, N. Bonini, E. Kioupakis, E. R. Margine, and F. Giustino, Electron-phonon physics from first principles using the EPW code, *npj Comput Mater* **9**, 156 (2023).

[38] P. Giannozzi, S. Baroni, N. Bonini, M. Calandra, R. Car, C. Cavazzoni, D. Ceresoli, G. L. Chiarotti, M. Cococcioni, I. Dabo, A. Dal Corso, S. de Gironcoli, S. Fabris, G. Fratesi, R. Gebauer, U. Gerstmann, C. Gougaoussis, A. Kokalj, M. Lazzeri, L. Martin-Samos, N. Marzari, F. Mauri, R. Mazzarello, S. Paolini, A. Pasquarello, L. Paulatto, C. Sbraccia, S. Scandolo, G. Sclauzero, A. P. Seitsonen, A. Smogunov, P. Umari, and R. M. Wentzcovitch, QUANTUM ESPRESSO: a modular and open-source software project for quantum simulations of materials, *Journal of Physics: Condensed Matter* **21**, 395502 (2009).

[39] P. Giannozzi, O. Andreussi, T. Brumme, O. Bunau, M. Buongiorno Nardelli, M. Calandra, R. Car, C. Cavazzoni, D. Ceresoli, M. Cococcioni, N. Colonna, I. Carnimeo, A. Dal Corso, S. de Gironcoli, P. Delugas, R. A. DiStasio, A. Ferretti, A. Floris, G. Fratesi, G. Fugallo, R. Gebauer, U. Gerstmann, F. Giustino, T. Gorni, J. Jia, M. Kawamura, H.-Y. Ko, A. Kokalj, E. Küçükbenli, M. Lazzeri, M. Marsili, N. Marzari, F. Mauri, N. L. Nguyen, H.-V. Nguyen, A. Otero-de-la Roza, L. Paulatto, S. Poncé, D. Rocca, R. Sabatini, B. Santra, M. Schlipf, A. P. Seitsonen, A. Smogunov, I. Timrov, T. Thonhauser, P. Umari, N. Vast, X. Wu, and S. Baroni, Advanced capabilities for materials modelling with quantum espresso, *Journal of Physics: Condensed Matter* **29**, 465901 (2017).

[40] P. Giannozzi, S. Baroni, N. Bonini, M. Calandra, R. Car, C. Cavazzoni, D. Ceresoli, G. L. Chiarotti, M. Cococcioni, I. Dabo, A. Dal Corso, S. De Gironcoli, S. Fabris, G. Fratesi, R. Gebauer, U. Gerstmann, C. Gougaoussis, A. Kokalj, M. Lazzeri, L. Martin-Samos, N. Marzari, F. Mauri, R. Mazzarello, S. Paolini, A. Pasquarello, L. Paulatto, C. Sbraccia, S. Scandolo, G. Sclauzero, A. P. Seitsonen, A. Smogunov, P. Umari, and R. M. Wentzcovitch, QUANTUM ESPRESSO: a modular and open-source software project for quantum simulations of materials, *Journal of Physics: Condensed Matter* **21**, 395502 (2009).

[41] P. Giannozzi, O. Andreussi, T. Brumme, O. Bunau, M. Buongiorno Nardelli, M. Calandra, R. Car, C. Cavazzoni, D. Ceresoli, M. Cococcioni, N. Colonna, I. Carnimeo, A. Dal Corso, S. De Gironcoli, P. Delugas, R. A. DiStasio, A. Ferretti, A. Floris, G. Fratesi, G. Fugallo, R. Gebauer, U. Gerstmann, F. Giustino, T. Gorni, J. Jia, M. Kawamura, H.-Y. Ko, A. Kokalj, E. Küçükbenli, M. Lazzeri, M. Marsili, N. Marzari, F. Mauri, N. L. Nguyen, H.-V. Nguyen, A. Otero-de-la Roza, L. Paulatto, S. Poncé, D. Rocca, R. Sabatini, B. Santra, M. Schlipf,

A. P. Seitsonen, A. Smogunov, I. Timrov, T. Thonhauser, P. Umari, N. Vast, X. Wu, and S. Baroni, Advanced capabilities for materials modelling with Quantum ESPRESSO, *Journal of Physics: Condensed Matter* **29**, 465901 (2017).

[42] J. P. Perdew, K. Burke, and M. Ernzerhof, Generalized gradient approximation made simple, *Phys. Rev. Lett.* **77**, 3865 (1996).

[43] J. P. Perdew, A. Ruzsinszky, G. I. Csonka, O. A. Vydrov, G. E. Scuseria, L. A. Constantin, X. Zhou, and K. Burke, Restoring the density-gradient expansion for exchange in solids and surfaces, *Phys. Rev. Lett.* **100**, 136406 (2008).

[44] M. Van Setten, M. Giantomassi, E. Bousquet, M. Verstraete, D. Hamann, X. Gonze, and G.-M. Rignanese, The PseudoDojo: Training and grading a 85 element optimized norm-conserving pseudopotential table, *Computer Physics Communications* **226**, 39 (2018).

[45] M. Methfessel and A. T. Paxton, High-precision sampling for brillouin-zone integration in metals, *Phys. Rev. B* **40**, 3616 (1989).

[46] P. Krål, J. N. Graham, V. Sazgari, I. Plokhikh, A. Lukovkina, O. Gerguri, I. Bialo, A. Doll, L. Martinelli, J. Oppliger, S. S. Islam, K. Wang, M. Salamin, H. Luetkens, R. Khasanov, M. v. Zimmermann, J. X. Yin, Z. Wang, J. Chang, B. Monserrat, D. Gawryluk, F. O. von Rohr, S. W. Kim, and Z. Guguchia, Discovery of High-Temperature Charge Order and Time-Reversal Symmetry-Breaking in the Kagome Superconductor YRu_3Si_2 (2025), arXiv:2507.06885.

[47] R. Misawa, S. Kitou, R. Yamada, T. Gaggl, R. Nakano, Y. Shibata, Y. Okamura, M. Kriener, P. R. Baral, Y. Nakamura, Y. Onuki, Y. Takahashi, T.-h. Arima, M. Jovanovic, L. M. Schoop, and M. Hirschberger, Successive Orthorhombic Distortions in Kagome Metals by Molecular Orbital Formation, *Advanced Materials* **e13015**, 1 (2025).

[48] M. I. Aroyo, J. M. Perez-Mato, D. Orobengoa, E. Tasci, G. de la Flor, and A. Kirov, Crystallography online: Bilbao crystallographic server, *Bulg. Chem. Commun.* **43**, 183 (2011).

[49] M. I. Aroyo, J. M. Perez-Mato, C. Capillas, E. Kroumova, S. Ivantchev, G. Madariaga, A. Kirov, and H. Wondratschek, Bilbao crystallographic server: I. databases and crystallographic computing programs, *Zeitschrift für Kristallographie-Crystalline Materials* **221**, 15 (2006).

[50] M. I. Aroyo, A. Kirov, C. Capillas, J. Perez-Mato, and H. Wondratschek, Bilbao crystallographic server. ii. representations of crystallographic point groups and space groups, *Acta Crystallographica Section A: Foundations of Crystallography* **62**, 115 (2006).

[51] W. L. McMillan, Transition temperature of strong-coupled superconductors, *Phys. Rev.* **167**, 331 (1968).

[52] R. Dynes, McMillan's equation and the T_c of superconductors, *Solid State Commun.* **10**, 615 (1972).

[53] P. B. Allen and R. C. Dynes, Transition temperature of strong-coupled superconductors reanalyzed, *Phys. Rev. B* **12**, 905 (1975).

[54] K.-E. Huhtinen, J. Herzog-Arbeitman, A. Chew, B. A. Bernevig, and P. Törmä, Revisiting flat band superconductivity: Dependence on minimal quantum metric and band touchings, *Phys. Rev. B* **106**, 014518 (2022).

[55] L. Liang, T. I. Vanhala, S. Peotta, T. Siro, A. Harju, and P. Törmä, Band geometry, berry curvature, and superfluid weight, *Phys. Rev. B* **95**, 024515 (2017).

[56] M. J. Winiarski, D. Walczak, S. Królak, D. Yazici, R. J. Cava, and T. Klimczuk, YRu_3B_2 - a kagome lattice superconductor, arXiv:2512.08514 <https://doi.org/10.48550/arXiv.2512.08514> (2025).

[57] T. Gaggl, R. Misawa, M. Kriener, Y. Tanaka, R. Yamada, and M. Hirschberger, Bulk superconductivity in the kagome metal YRu_3B_2 , arXiv:2512.09314 <https://doi.org/10.48550/arXiv.2512.09314> (2025).